Physics of Fluids

Band broadening in mobility shift affinity capillary electrophoresis due to pressure-driven flow

Cite as: Phys. Fluids **33**, 103602 (2021); https://doi.org/10.1063/5.0062701
Submitted: 07 July 2021 • Accepted: 10 September 2021 • Published Online: 01 October 2021

Debashis Dutta

Physics of Fluids ARTICLE scitation.org/journal/phf

Band broadening in mobility shift affinity capillary electrophoresis due to pressure-driven flow

Cite as: Phys. Fluids **33**, 103602 (2021); doi: 10.1063/5.0062701
Submitted: 7 July 2021 · Accepted: 10 September 2021 ·
Published Online: 1 October 2021

Debashis Dutta[a]

AFFILIATIONS

Department of Chemistry, University of Wyoming, 1000 East University Avenue, Laramie, Wyoming 82071, USA

[a]Author to whom correspondence should be addressed: ddutta@uwyo.edu. Phone: (307) 766-4318. Fax: (307) 766-2807

ABSTRACT

Mobility Shift Affinity Capillary Electrophoresis (msACE) presents a simple and powerful approach to determining the equilibrium and kinetic parameters governing the interaction between a variety of analyte and ligand molecules. These determinations often rely on measuring the elution peak profile for the analyte zone when migrated with a steady electric field. However, pressure-gradients applied intentionally or generated due to unwanted differences in the hydrostatic heads at the capillary/channel ends and/or a variation in the electroosmotic flow rate along the analysis column can significantly alter this peak profile introducing error in the estimated parameter values. To account for these alterations, this article describes a mathematical formulation for quantitating band broadening in msACE systems due to a steady pressure-driven flow in the Taylor–Aris dispersion limit with fast analyte-ligand binding kinetics. The current analysis shows that the additional zone dispersion under such conditions can be quantitated using four terms that scale with the square of the Péclet number calculated based on the pressure-driven flow velocity. While the first term among these quantitates the Taylor–Aris dispersion experienced by a neutral tracer advected by the pressure-gradient, the other three terms are proportional to the square of the difference in the diffusion coefficients for the analyte and analyte-ligand complex. Moreover, these latter terms also vary inversely with the Damköhler number computed as the ratio of the rate of reaction over that of diffusive mass transfer with the coefficient for each of the four terms shown to be dependent on the cross-sectional shape of the analysis column.

I. INTRODUCTION

Measurements of equilibrium and kinetic parameters governing affinity interactions are of paramount importance to understanding a wide range of chemical and biological systems.[1,2] A variety of techniques are used to make these measurements including fluorescence spectroscopy, (cryo-) electron microscopy, isothermal titration calorimetry, surface plasmon resonance, nuclear magnetic resonance, and capillary electrophoresis (CE). Among these approaches, CE offers the ability to conveniently measure affinity interactions at the level of a few molecules, single cells, between cells, and even individual organisms. These opportunities primarily arise due to a lack of convective mixing between the bound and unbound species in CE assays particularly when performed in capillaries/channels with lateral dimensions on the order of 100 μm or narrower.[2] Additionally, the CE approach can allow the extraction of more specific and accurate binding details such as interaction sites, binding stoichiometry, binding constants, etc., which are helpful in better understanding the molecular mechanisms of basic processes.[3] Furthermore, CE determinations can be performed under physiologically relevant conditions, which makes them particularly suitable for studies of biomolecular interactions.

Mobility Shift Affinity Capillary Electrophoresis (msACE) is among the most extensively used method for making affinity measurements employing the CE approach.[4] In this method, the analyte is introduced into an analysis column filled with a background electrolyte containing different concentrations of the ligand. Fast on and off kinetics are desired in these assays to allow chemical equilibration of the analyte and ligand on a timescale that is significantly shorter than that required by the analyze analyte zone to migrate through the column. This near equilibrium condition is typically realized using ligand concentrations 1–2 orders of magnitude larger than that of the analyte. A large excess of the ligand in the background electrolyte also ensures that the spatial and temporal variations in its concentration across the analyte zone are negligible irrespective of the extent of analyte-ligand equilibration at any location. While this format for the msACE method works well for reliable determination of interaction parameters for a variety of analyte-ligand couples, it also has some important limitations.[5,6] For example, increasing the ligand concentration can

produce a change in viscosity and ionic strength of the background electrolyte that needs to be corrected to minimize errors in the estimated interaction parameters. Also, high concentrations of the analyte are desired in msACE analysis to help obtain sufficient signal but that approach can introduce significant deviations from the equilibrium condition and produce local variations in the ligand concentration. Finally, adsorption of analyte and/or ligand onto the capillary/channel wall can affect the peak migration and/or width/shape introducing errors in the estimated parameter values. As a result, wall coatings are often used to minimize such adsorption as well as improve the reproducibility of the assay.

Some recent studies have shown that careful analysis of the peak widths and shapes in conjunction with information on their elution times in an msACE assay can allow reliable determination of several equilibrium and kinetic parameters governing affinity interactions.[7–11] For example, Miyabe and co-workers applied the method-of-moments approach to estimate both equilibrium and rate constants using information on the velocity and width of the analyte zone.[11] Their work relied on theoretical models that described peak migration and dispersion under the influence of a steady axial electric field but in the absence of more complicated operating conditions and/or other non-idealities, e.g., pressure-gradients, Joule heating, etc. In order to realize the full potential of the msACE method however, theoretical models capable of describing these systems under more realistic and complex experimental situations are desirable enabling estimation of the interaction parameters with greater reliability than currently possible.

In an effort to accomplish that overall goal, the current article expands on the method-of-moments approach[12] to describe peak migration and dispersion in msACE systems in the presence of a steady pressure-driven flow. It must be noted that such flows can originate from unwanted differences in the hydrostatic heads at the capillary/channel ends and/or a variation in the electroosmotic flow rate along the analysis column. Moreover, steady pressure-gradients are also intentionally applied during affinity measurements in assays that are variants of the msACE technique. For example, equilibrium and kinetic parameters were recently estimated based on a chromatographic capillary electrophoretic assay applying a pressure-driven backflow to prevent the analyte-ligand complex from migrating through the analysis column.[13] The current analysis shows that while the peak migration rate under these conditions is simply altered by the area-averaged pressure-driven velocity, the peak dispersion exhibits a more complex behavior. Although the additional band broadening from a steady pressure-gradient in an msACE assay scales with the square of the Péclet number in the Taylor–Aris dispersion limit as in most pressure-driven flow systems, the coefficient multiplying it depends on the kinetic rate constants, molecular diffusivities, lateral channel dimensions, and cross-sectional shape of the analysis column.

II. MATHEMATICAL FORMULATION

To examine the effect of a steady pressure-driven flow on the peak velocity and width in an msACE assay, this article considers analyte transport between two parallel plates separated by a distance d and through a cylindrical tube having the same diameter (see Fig. 1). Advection in these analysis columns is driven by a combination of electrokinetic and pressure-driven flows along the column axis (z-coordinate) induced by an electric field (E) and pressure-drop (ΔP), respectively. Representing lateral positions using the y-coordinate in the

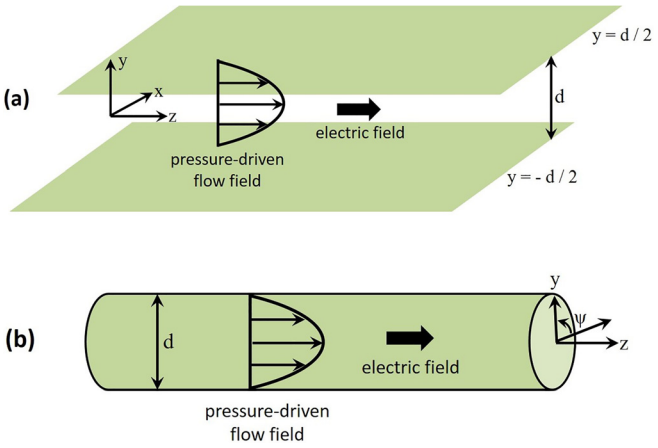

FIG. 1. Schematic of the (a) parallel-plate and (b) cylindrical tube device used for performing msACE assays described in this article. Notice that the symbol ψ in sub-figure (b) refers to the azimuth angle in the cylindrical coordinate system which in this analysis does not influence any of the transport properties due to symmetry about the z-axis.

system, the channel walls in the parallel plate and cylindrical tube geometries are further assumed to be located at $y = \pm d/2$ and $y = d/2$, respectively, to produce liquid flow and analyte concentration profiles that are both symmetric about $y = 0$.[14] The binding of the analyte (S) to the ligand (L) to form a complex (X) is represented by the reaction $S + L \underset{k_d}{\overset{k_a}{\rightleftharpoons}} X$ in this work where k_a and k_d denote the rate constants for the forward and reverse reactions, respectively. Because the current analysis considers the ligand to be present in the background electrolyte at a concentration L_0 which significantly exceeds that of the analyte, the pseudo first-order equilibrium constant $K_{eq} = k_a L_0/k_d$ for the binding reaction is assumed to be spatially and temporally uniform in the system. In this situation, the advection-diffusion equations governing the concentration profile for the analyte (C_S) and analyte-ligand complex (C_X) may be written as[15]

$$\begin{aligned}
\frac{\partial C_S}{\partial t} &= \frac{D_S}{y^n}\frac{\partial}{\partial y}\left(y^n \frac{\partial C_S}{\partial y}\right) + D_S\frac{\partial^2 C_S}{\partial z^2} - U_S\frac{\partial C_S}{\partial z} \\
&\quad - \frac{(3+n)}{2}U_p\left(1 - \frac{4y^2}{d^2}\right)\frac{\partial C_S}{\partial z} - k_a L_0 C_S + k_d C_X, \\
\frac{\partial C_X}{\partial t} &= \frac{D_X}{y^n}\frac{\partial}{\partial y}\left(y^n \frac{\partial C_X}{\partial y}\right) + D_X\frac{\partial^2 C_X}{\partial z^2} - U_X\frac{\partial C_X}{\partial z} \\
&\quad - \frac{(3+n)}{2}U_p\left(1 - \frac{4y^2}{d^2}\right)\frac{\partial C_X}{\partial z} + k_a L_0 C_S - k_d C_X. \qquad (1)
\end{aligned}$$

$$\text{Boundary conditions}: \left.\frac{\partial C_S}{\partial y}\right|_{y=0,\frac{d}{2}} = \left.\frac{\partial C_X}{\partial y}\right|_{y=0,\frac{d}{2}} = 0,$$

$$C_S,\ C_X,\ \frac{\partial^j C_S}{\partial z^j},\quad \frac{\partial^j C_X}{\partial z^j} \to 0 \quad \text{as } z \to \pm\infty \text{ for } j = 1, 2, \ldots,$$

$$\text{at } t = 0, \quad C_S = \frac{C_0}{1+K_{eq}}; \quad C_X = \frac{K_{eq}C_0}{1+K_{eq}} \text{ for } -\frac{b}{2} \le z \le \frac{b}{2};$$

$$C_S = C_X = 0 \text{ elsewhere.}$$

Here, U_p denotes the pressure-driven flow velocity averaged over the capillary/channel cross-sectional area, t represents the time coordinate, and while D_S and D_X correspond to the molecular diffusion coefficients for the analyte and analyte-ligand complex, respectively. The spatially uniform electrokinetic (algebraic sum of the electroosmotic and electrophoretic components) velocity for the species S and X has been identified by the parameters U_S and U_X in these equations with $n = 0$ and $n = 1$ representing the parallel-plate and cylindrical tube cases, respectively. The quantity C_0 here represents the concentration of S in the bulk sample. Notice that the pressure-driven flow-field considered in this work is one-dimensional in nature as it varies with only the y-coordinate in the system. Upon normalizing all length scales with respect to d, i.e., $y^*, z^* = y/d, z/d$, the time coordinate with respect to the diffusion timescale for S, i.e., $t^* = D_S t/d^2$, and the concentrations by the quantity C_0, i.e., C_S^*, $C_X^* = C_S/C_0$, C_X/C_0, Eq. (1) may be rewritten as

$$\frac{\partial C_S^*}{\partial t^*} = \frac{1}{y^{*n}}\frac{\partial}{\partial y^*}\left(y^{*n}\frac{\partial C_S^*}{\partial y^*}\right) + \frac{\partial^2 C_S^*}{\partial z^{*2}} - Pe_S\frac{\partial C_S^*}{\partial z^*} - \frac{(3+n)}{2}Pe_p\left(1-4y^{*2}\right)\frac{\partial C_S^*}{\partial z^*} - Da\left(K_{eq}C_S^* - C_X^*\right),$$

$$\frac{\partial C_X^*}{\partial t^*} = \frac{\alpha}{y^{*n}}\frac{\partial}{\partial y^*}\left(y^{*n}\frac{\partial C_X^*}{\partial y^*}\right) + \alpha\frac{\partial^2 C_X^*}{\partial z^{*2}} - \alpha Pe_X\frac{\partial C_X^*}{\partial z^*} - \frac{(3+n)}{2}Pe_p\left(1-4y^{*2}\right)\frac{\partial C_X^*}{\partial z^*} + Da\left(K_{eq}C_S^* - C_X^*\right). \quad (2)$$

Boundary conditions: $\left.\frac{\partial C_S^*}{\partial y^*}\right|_{y^*=0,\frac{1}{2}} = \left.\frac{\partial C_X^*}{\partial y^*}\right|_{y^*=0,\frac{1}{2}} = 0,$

$$C_S^*,\ C_X^*,\ \frac{\partial^j C_S^*}{\partial z^{*j}},\ \frac{\partial^j C_X^*}{\partial z^{*j}} \to 0 \quad \text{as } z^* \to \pm\infty \text{ for } j = 1, 2, \ldots,$$

at $t^* = 0$, $\quad C_S^* = \frac{1}{1+K_{eq}}; \quad C_X^* = \frac{K_{eq}}{1+K_{eq}}$ for $-\frac{\delta}{2} \le z^* \le \frac{\delta}{2};$

$$C_S^* = C_X^* = 0 \text{ elsewhere.}$$

The quantities $Pe_S = U_S d/D_S$, $Pe_X = U_X d/D_X$, and $Pe_p = U_p d/D_S$ here refer to the different Péclet numbers relevant to this analysis with $Da = k_d d^2/D_S$ denoting the Damköhler number for the system.[16] It must be pointed out that while there is no preference to normalizing the timescale with respect to D_S or D_X, the former option was chosen for this analysis. The parameter α in Eq. (2) denotes the ratio of the molecular diffusion coefficients D_X/D_S and typically assumes values less than 1 due to a larger molecular weight of X compared to that of S. Notice that the current work considers laminar flow in the system and is therefore valid for small Reynolds numbers. In this limit, fluid inertia does not play a role in material transport but molecular diffusion does. As a result, the Péclet number becomes a key non-dimensional input parameter in this analysis rather than Reynolds number. Now multiplying Eq. (2) with z^{*k} followed by integrating it along the z^*-coordinate from $-\infty$ to ∞, it is possible to show that[12]

$$\frac{\partial \phi_k^S}{\partial t^*} = \frac{1}{y^{*n}}\frac{\partial}{\partial y^*}\left(y^{*n}\frac{\partial \phi_k^S}{\partial y^*}\right) + k(k-1)\phi_{k-2}^S + kPe_S\phi_{k-1}^S + \frac{(3+n)}{2}kPe_p\left(1-4y^{*2}\right)\phi_{k-1}^S - Da\left(K_{eq}\phi_k^S - \phi_k^X\right),$$

$$\frac{\partial \phi_k^X}{\partial t^*} = \frac{\alpha}{y^{*n}}\frac{\partial}{\partial y^*}\left(y^{*n}\frac{\partial \phi_k^X}{\partial y^*}\right) + \alpha k(k-1)\phi_{k-2}^X + \alpha kPe_X\phi_{k-1}^X + \frac{(3+n)}{2}kPe_p\left(1-4y^{*2}\right)\phi_{k-1}^X + Da\left(K_{eq}\phi_k^S - \phi_k^X\right). \quad (3)$$

Boundary conditions: $\left.\frac{\partial \phi_k^S}{\partial y^*}\right|_{y^*=0,\frac{1}{2}} = \left.\frac{\partial \phi_k^X}{\partial y^*}\right|_{y^*=0,\frac{1}{2}} = 0.$

Initial conditions at $t^* = 0$ $\quad \phi_0^S + \phi_0^X = 1;$

$$\phi_1^S + \phi_1^X = 0; \quad \phi_2^S + \phi_2^X = \frac{\delta^2}{12},$$

where $\phi_k^S = \int_{-\infty}^{\infty} C_S^* z^{*k} dz^*$ and $\phi_k^X = \int_{-\infty}^{\infty} C_X^* z^{*k} dz^*$. Further integrating Eq. (3) along the y^*-coordinate and defining $m_k^S = 2\pi^n \int_0^{1/2} \phi_k^S y^{*n} dy^*$ and $m_k^X = 2\pi^n \int_0^{1/2} \phi_k^X y^{*n} dy^*$ one can obtain

$$\frac{dm_k^S}{dt^*} = k(k-1)m_{k-2}^S + kPe_S m_{k-1}^S + (3+n)\pi^n kPe_p\int_0^{1/2}\left(1-4y^{*2}\right)y^{*n}\phi_{k-1}^S dy^* - Da\left(K_{eq}m_k^S - m_k^X\right),$$

$$\frac{dm_k^X}{dt^*} = \alpha k(k-1)m_{k-2}^X + \alpha kPe_X m_{k-1}^X + (3+n)\pi^n kPe_p\int_0^{1/2}\left(1-4y^{*2}\right)y^{*n}\phi_{k-1}^X dy^* + Da\left(K_{eq}m_k^S - m_k^X\right). \quad (4)$$

Initial conditions at $t^* = 0$ $\quad m_0^S + m_0^X = 1;$

$$m_1^S + m_1^X = 0; \quad m_2^S + m_2^X = \frac{\delta^2}{12},$$

where $\delta = b/d$ and the sample is assumed to be spread uniformly over a zone of width b at $t^* = 0$. Notice that m_k^S and m_k^X in this formulation represent the kth moment of C_S^* and C_X^*, respectively, along the z^*-coordinate after spatially averaging over the y^* domain. In this situation, $m_1^S + m_1^X$ quantifies the normalized z^*-position for the center of mass of the sample zone, and $\left(m_2^S + m_2^X\right) - \left(m_1^S + m_1^X\right)^2$ equals its normalized spatial variance along the z-axis.[17–19]

Besides seeking analytical solutions for band broadening in msACE systems with a steady pressure-driven flow, numerical simulations using the COMSOL Multiphysics package were also performed to validate these results as well as establish the timescale over which the analytical predictions are applicable. These simulations involved numerically solving Eq. (1) applying the relevant boundary and initial conditions for a fully developed flow field. To simplify the analysis, a parallel plate system separated by a unit distance and a cylindrical tube with a unit diameter were chosen in the simulations with the domain extending 2000 units along the direction of analyte flow ($0 \le z^* \le 2000$). Moreover, the spatial variance of the injected zone of S was chosen to be at least 10^4 times smaller than its steady state

value at the channel outlet as predicted by the analytical model to render this contribution to band broadening negligible relative to other sources. A zone of X in equilibrium with S was also introduced in these simulations and its transport tracked based on Eq. (1). Furthermore, the spatial extent of the separation chamber along the z-direction was chosen to be at least 8 times larger than the product of the axial velocity of S, i.e., $U_S + U_p$, and the characteristic diffusion timescale $\left(d^2/4D_S\right)$ in the system to ensure that the zone width at the channel exit corresponded to the result in the Taylor–Aris dispersion limit.

III. RESULTS AND DISCUSSION

The current analysis focuses on the mathematical solutions for Eq. (4) when $k = 0$, 1, and 2 to understand zone migration and broadening in msACE systems with fast on and off binding kinetics, i.e., Da, $K_{eq}Da \gtrsim 1$ in the Taylor–Aris dispersion limit,[12,20] i.e., $t^* \gg 1$. Under these conditions, it may be shown that

$$m_0^S = \frac{1}{1+K_{eq}}; \quad \phi_0^S = \left(\frac{4}{\pi}\right)^n \frac{1}{1+K_{eq}} \quad \text{and} \quad m_0^X = \frac{K_{eq}}{1+K_{eq}}; \quad \phi_0^X = \left(\frac{4}{\pi}\right)^n \frac{K_{eq}}{1+K_{eq}}. \tag{5}$$

The above expressions simply correspond to the steady state solutions for Eqs. (3) and (4) when $k = 0$ establishing that the amounts of S and X to be temporally invariant in this time limit. Moreover, these solutions show that the fraction of S present as analyte-ligand complex (X) increases with K_{eq} approaching a value of 1 when $K_{eq} \to \infty$ (see Fig. 2). Additionally, ϕ_0^S and ϕ_0^X are found to be spatially uniform implying that the amount of material present along any flow streamline to be the same under these conditions. Further analysis reveals that the time dependent component of these solutions decays as $e^{-Da(1+K_{eq})t^*}$ implying that the temporal variation in m_0^S and m_0^X cannot be neglected for $t^* \lesssim 1/[Da(1+K_{eq})]$.[21] At these shorter time scales, the dependence of ϕ_0^S and ϕ_0^X on the y^*-coordinate can also be significant leading to a more complicated description of analyte transport in the system. It must be pointed out though that the solutions for m_0^S and m_0^X included in Eq. (5) are identical for the parallel-plate $(n = 0)$ and cylindrical tube $(n = 1)$ geometries as the total amount of sample introduced into them was chosen to be the same in this analysis. The steady state solutions for ϕ_0^S and ϕ_0^X, however, are found to be dependent on the cross-sectional area of the analysis column yielding the $4/\pi$ factor in Eq. (5). This factor corresponds to the ratio of the cross-sectional area between two parallel-plates of unit width separated by a distance d over that of a cylindrical capillary of diameter d.

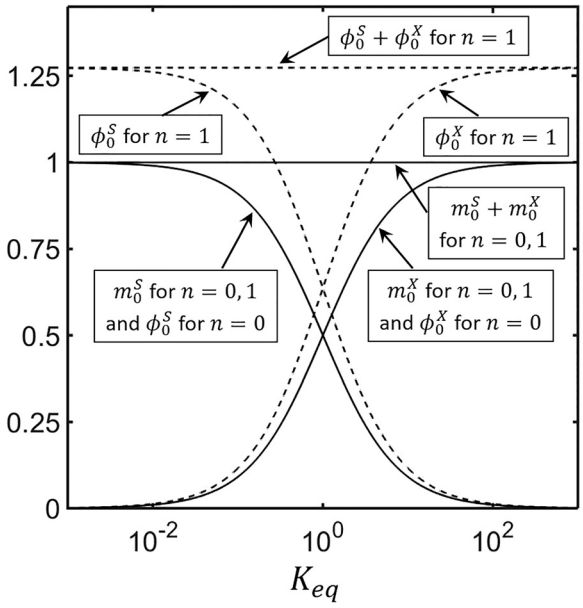

FIG. 2. Variation in the zeroth-order moment of concentration for S and X, i.e., m_0^S and m_0^X, with the pseudo first-order equilibrium constant (K_{eq}) during an msACE assay as considered in this work when performed in a parallel-plate ($n = 0$) and a cylindrical tube ($n = 1$) device. Notice that the quantities ϕ_0^S and ϕ_0^X equal m_0^S and m_0^X, respectively, for a parallel-plate device but not for a cylindrical tube upon setting $m_0^S + m_0^X = 1$ in both cases.

For $k = 1$, Eq. (4) may be solved in the Taylor–Aris dispersion limit to yield

$$m_1^S = \left[\frac{Pe_S + \alpha K_{eq} Pe_X}{(1+K_{eq})^2} + \frac{Pe_p}{1+K_{eq}}\right] t^* + \frac{K_{eq}(Pe_s - \alpha Pe_X)}{Da(1+K_{eq})^3},$$
$$m_1^X = \left[\frac{K_{eq}(Pe_S + \alpha K_{eq} Pe_X)}{(1+K_{eq})^2} + \frac{K_{eq} Pe_p}{1+K_{eq}}\right] t^* - \frac{K_{eq}(Pe_s - \alpha Pe_X)}{Da(1+K_{eq})^3}, \tag{6}$$
$$m_1^S + m_1^X = \left(\frac{Pe_S + \alpha K_{eq} Pe_X}{1+K_{eq}} + Pe_p\right) t^*,$$

which show that at this timescale the centers of mass for S and X migrate with steady velocities $u_S = dm_1^S/dt^*$ and $u_X = dm_1^X/dt^*$, respectively, such that $u_X = K_{eq} u_S$. As a result, u_X is always greater u_S when $K_{eq} > 1$ and vice versa, irrespective of the magnitude of the molecular velocities for these two species (U_S and U_X). The migration speed for the combined sample zone under these conditions is given by $d\left(m_1^S + m_1^X\right)/dt^*$ and may be expressed as the weighted average of the electrokinetic transport rate for S and X plus the pressure-driven flow speed averaged over the cross-sectional area of the channel/capillary. Now because the electrokinetic velocities for the analyte and analyte-ligand complex as well as the pressure-driven flow speed were chosen to be identical for the parallel-plate device and cylindrical capillary in Eqs. (3) and (4), the solutions included in Eq. (6) turn out to be the same for $n = 0$ and n = 1. The above results also show that while u_S approaches a value of $Pe_S + Pe_p$ when $K_{eq} \to 0$, this quantity diminishes to zero in the limit of $K_{eq} \to \infty$ [see Fig. 3(a)]. The quantity u_X on the other hand assumes a value of zero when $K_{eq} = 0$ and asymptotes to $\alpha Pe_X + Pe_p$ in the limit of $K_{eq} \to \infty$. Interestingly however, although u_S decreases monotonically for larger values of K_{eq} in all the situations considered in this analysis, the variation of u_X with the pseudo first-order equilibrium constant is monotonic only when $Pe_p + 2\alpha Pe_X \geq Pe_S$. Under conditions when $Pe_S > Pe_p + 2\alpha Pe_X$, the migration velocity of X rises steadily upon increasing K_{eq} but then exhibits a weak maximum at $K_{eq} = Pe_S - Pe_p - 2\alpha Pe_X$ before plateauing to its asymptotic value corresponding to the limit $K_{eq} \to \infty$.

In the Taylor–Aris dispersion limit, Eq. (6) further indicates that the centers of mass for S and X are projected to be offset from that of the combined sample zone in opposite directions at the initial time. The normalized value for this offset distance is simply the magnitude of m_1^S at $t^* = 0$ given by $\Delta z_0 = K_{eq}(Pe_s - \alpha Pe_X)/\left[Da(1+K_{eq})^3\right]$ with the center of mass for S leading that of X when $Pe_S > \alpha Pe_X$, and vice versa. Note that the quantity Δz_0 vanishes in the limit of Da and K_{eq} approaching infinity as it originates from the finite values of the

rate constants in the system. In fact, this offset distance scales linearly with $(Pe_S - \alpha Pe_X)/Da$ which is the separation gap produced by the differential in the molecular velocities for S and X, i.e., $Pe_S - \alpha Pe_X$, over the reaction timescale $(1/Da)$. In Fig. 3(b), the variation in the noted separation gap between the centers of mass for S and X, i.e., $2\Delta z_0$, with K_{eq} has been included which shows this quantity to decline to zero both when $K_{eq} \to 0$ or ∞, and assume a maximum value of $8(Pe_S - \alpha Pe_X)/(27Da)$ at $K_{eq} = 1/2$. In addition, this separation gap is found to be independent of the channel/capillary cross-sectional shape or its area yielding identical values for $n = 0$ and $n = 1$ under conditions considered in this analysis.

In the Taylor–Aris dispersion limit, Eq. (3) may also be solved to obtain analytical solutions for ϕ_1^S and ϕ_1^X yielding the result below for a parallel-plate device

$$\begin{aligned}
\phi_1^S &= \left[\frac{Pe_S + \alpha Pe_X}{(1+K_{eq})^2} + \frac{Pe_p}{1+K_{eq}}\right] t^* - \frac{6\alpha(1-\alpha)K_{eq}Pe_p \cosh(\lambda y^*)}{\lambda \sinh(\lambda/2) Da (1+K_{eq})(1+\alpha K_{eq})^2} + \frac{Pe_p y^{*4}}{2(1+\alpha K_{eq})} \\
&\quad + \left[\frac{6\alpha(1-\alpha)K_{eq}Pe_p}{Da(1+K_{eq})(1+\alpha K_{eq})^2} - \frac{Pe_p}{4(1+\alpha K_{eq})}\right] y^{*2} + \frac{7Pe_p}{480(1+\alpha K_{eq})} + \frac{K_{eq}(Pe_S - \alpha Pe_X)}{Da(1+K_{eq})^3} \\
&\quad - \frac{\alpha(1-\alpha)K_{eq}Pe_p}{2Da(1+K_{eq})(1+\alpha K_{eq})^2} + \frac{12\alpha^2(1-\alpha)K_{eq}Pe_p}{Da^2(1+K_{eq})(1+\alpha K_{eq})^3}, \\
\phi_1^X &= K_{eq}\left[\frac{Pe_S + \alpha Pe_X}{(1+K_{eq})^2} + \frac{Pe_p}{1+K_{eq}}\right] t^* + \frac{6(1-\alpha)K_{eq}Pe_p \cosh(\lambda y^*)}{\lambda \sinh(\lambda/2) Da (1+K_{eq})(1+\alpha K_{eq})^2} + \frac{K_{eq}Pe_p y^{*4}}{2(1+\alpha K_{eq})} \\
&\quad - \left[\frac{6(1-\alpha)K_{eq}Pe_p}{Da(1+K_{eq})(1+\alpha K_{eq})^2} + \frac{K_{eq}Pe_p}{4(1+\alpha K_{eq})}\right] y^{*2} + \frac{7K_{eq}Pe_p}{480(1+\alpha K_{eq})} - \frac{K_{eq}(Pe_S - \alpha Pe_X)}{Da(1+K_{eq})^3} \\
&\quad + \frac{(1-\alpha)K_{eq}Pe_p}{2Da(1+K_{eq})(1+\alpha K_{eq})^2} - \frac{12\alpha(1-\alpha)K_{eq}Pe_p}{Da^2(1+K_{eq})(1+\alpha K_{eq})^3}, \\
\phi_1^S + \phi_1^X &= \left[\frac{Pe_S + \alpha Pe_X}{1+K_{eq}} + Pe_p\right] t^* + \frac{6(1-\alpha)^2 K_{eq}Pe_p \cosh(\lambda y^*)}{\lambda \sinh(\lambda/2) Da (1+K_{eq})(1+\alpha K_{eq})^2} + \frac{(1+K_{eq})Pe_p y^{*4}}{2(1+\alpha K_{eq})} \\
&\quad - \left[\frac{6(1-\alpha)^2 K_{eq}Pe_p}{Da(1+K_{eq})(1+\alpha K_{eq})^2} + \frac{(1+K_{eq})Pe_p}{4(1+\alpha K_{eq})}\right] y^{*2} + \frac{7(1+K_{eq})Pe_p}{480(1+\alpha K_{eq})} + \frac{(1-\alpha)^2 K_{eq}Pe_p}{2Da(1+K_{eq})(1+\alpha K_{eq})^2} - \frac{12\alpha(1-\alpha)^2 K_{eq}Pe_p}{Da^2(1+K_{eq})(1+\alpha K_{eq})^3},
\end{aligned} \tag{7}$$

where $= \sqrt{Da(1+\alpha K_{eq})/\alpha}$. The corresponding solutions for a cylindrical capillary are

$$\begin{aligned}
\phi_1^S &= \frac{4}{\pi}\left[\frac{Pe_S + \alpha Pe_X}{(1+K_{eq})^2} + \frac{Pe_p}{1+K_{eq}}\right] t^* - \frac{32\alpha(1-\alpha)K_{eq}Pe_p I_0(\lambda y^*)}{\lambda \pi I_1(\lambda/2) Da (1+K_{eq})(1+\alpha K_{eq})^2} + \frac{2Pe_p y^{*4}}{\pi(1+\alpha K_{eq})} \\
&\quad + \frac{1}{\pi}\left[\frac{32\alpha(1-\alpha)K_{eq}Pe_p}{Da(1+K_{eq})(1+\alpha K_{eq})^2} - \frac{Pe_p}{(1+\alpha K_{eq})}\right] y^{*2} + \frac{Pe_p}{12\pi(1+\alpha K_{eq})} + \frac{4K_{eq}(Pe_S - \alpha Pe_X)}{\pi Da(1+K_{eq})^3} \\
&\quad - \frac{4\alpha(1-\alpha)K_{eq}Pe_p}{\pi Da(1+K_{eq})(1+\alpha K_{eq})^2} + \frac{128\alpha^2(1-\alpha)K_{eq}Pe_p}{\pi Da^2(1+K_{eq})(1+\alpha K_{eq})^3}, \\
\phi_1^X &= \frac{4}{\pi}\left[\frac{K_{eq}(Pe_S + \alpha Pe_X)}{(1+K_{eq})^2} + \frac{K_{eq}Pe_p}{1+K_{eq}}\right] t^* + \frac{32(1-\alpha)K_{eq}Pe_p I_0(\lambda y^*)}{\lambda \pi I_1(\lambda/2) Da (1+K_{eq})(1+\alpha K_{eq})^2} + \frac{2K_{eq}Pe_p y^{*4}}{\pi(1+\alpha K_{eq})} \\
&\quad - \frac{1}{\pi}\left[\frac{32(1-\alpha)K_{eq}Pe_p}{Da(1+K_{eq})(1+\alpha K_{eq})^2} + \frac{K_{eq}Pe_p}{(1+\alpha K_{eq})}\right] y^{*2} + \frac{K_{eq}Pe_p}{12\pi(1+\alpha K_{eq})} - \frac{4K_{eq}(Pe_S - \alpha Pe_X)}{\pi Da(1+K_{eq})^3} \\
&\quad + \frac{4(1-\alpha)K_{eq}Pe_p}{\pi Da(1+K_{eq})(1+\alpha K_{eq})^2} - \frac{128\alpha(1-\alpha)K_{eq}Pe_p}{\pi Da^2(1+K_{eq})(1+\alpha K_{eq})^3}, \\
\phi_1^S + \phi_1^X &= \frac{4}{\pi}\left[\frac{Pe_S + \alpha Pe_X}{1+K_{eq}} + Pe_p\right] t^* + \frac{32(1-\alpha)^2 K_{eq}Pe_p I_0(\lambda y^*)}{\lambda \pi I_1(\lambda/2) Da (1+K_{eq})(1+\alpha K_{eq})^2} + \frac{2(1+K_{eq})Pe_p y^{*4}}{\pi(1+\alpha K_{eq})} \\
&\quad - \frac{1}{\pi}\left[\frac{32(1-\alpha)^2 K_{eq}Pe_p}{Da(1+K_{eq})(1+\alpha K_{eq})^2} + \frac{(1+K_{eq})Pe_p}{(1+\alpha K_{eq})}\right] y^{*2} + \frac{(1+K_{eq})Pe_p}{12\pi(1+\alpha K_{eq})} + \frac{4(1-\alpha)^2 K_{eq}Pe_p}{\pi Da(1+K_{eq})(1+\alpha K_{eq})^2} \\
&\quad - \frac{128\alpha(1-\alpha)^2 K_{eq}Pe_p}{\pi Da^2(1+K_{eq})(1+\alpha K_{eq})^3},
\end{aligned} \tag{8}$$

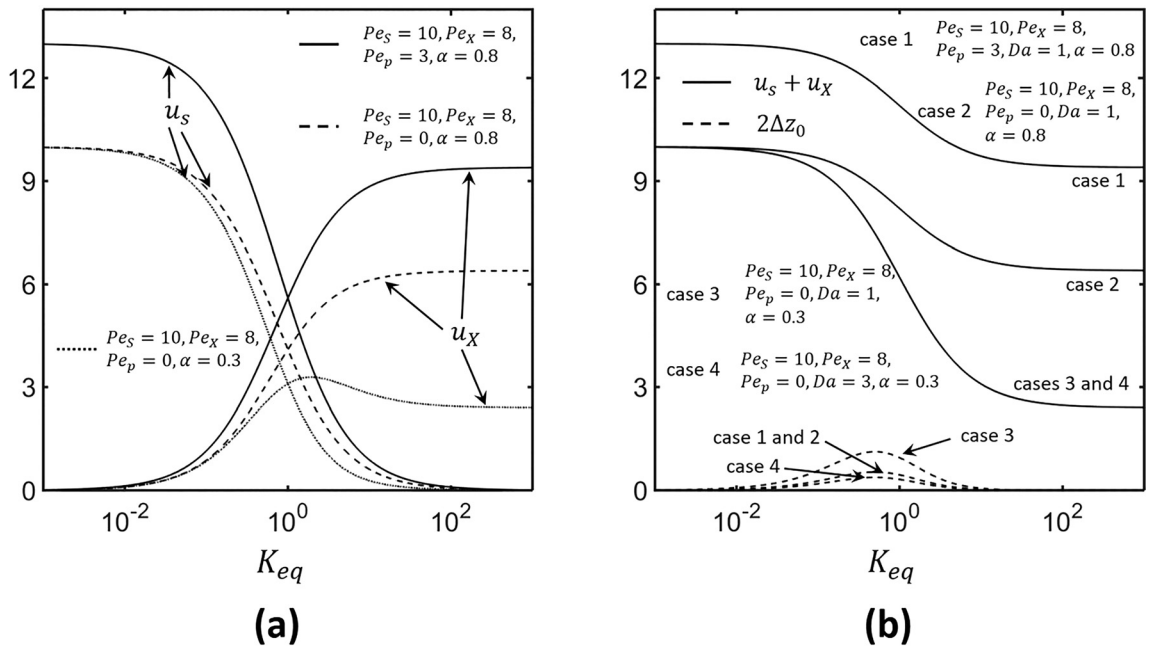

FIG. 3. (a) Variation in the migration velocity for S and X, i.e., u_S and u_X, with the pseudo first-order equilibrium constant (K_{eq}) under various operating conditions during an msACE assay. (b) Variation in the migration velocity of the combined sample zone, i.e., $u_S + u_X$, with the pseudo first-order equilibrium constant (K_{eq}) under various operating conditions during an msACE assay. The results included in both the sub-figures are identical for a parallel-plate device ($n = 0$) and cylindrical tube ($n = 1$) in this analysis.

where I_0 and I_1 refer to the zeroth and first order modified Bessel functions, respectively. The solutions for ϕ_1^S and ϕ_1^X included in Eqs. (7) and (8) show that these quantities have a spatial dependence on the y^*-coordinate which interestingly only appears in the terms that are independent of t^*. Moreover, these quantities are functions of both the cross-sectional shape and area yielding somewhat different results for the parallel-plate device and cylindrical capillary. The time-dependent terms however are only influenced by the cross-sectional

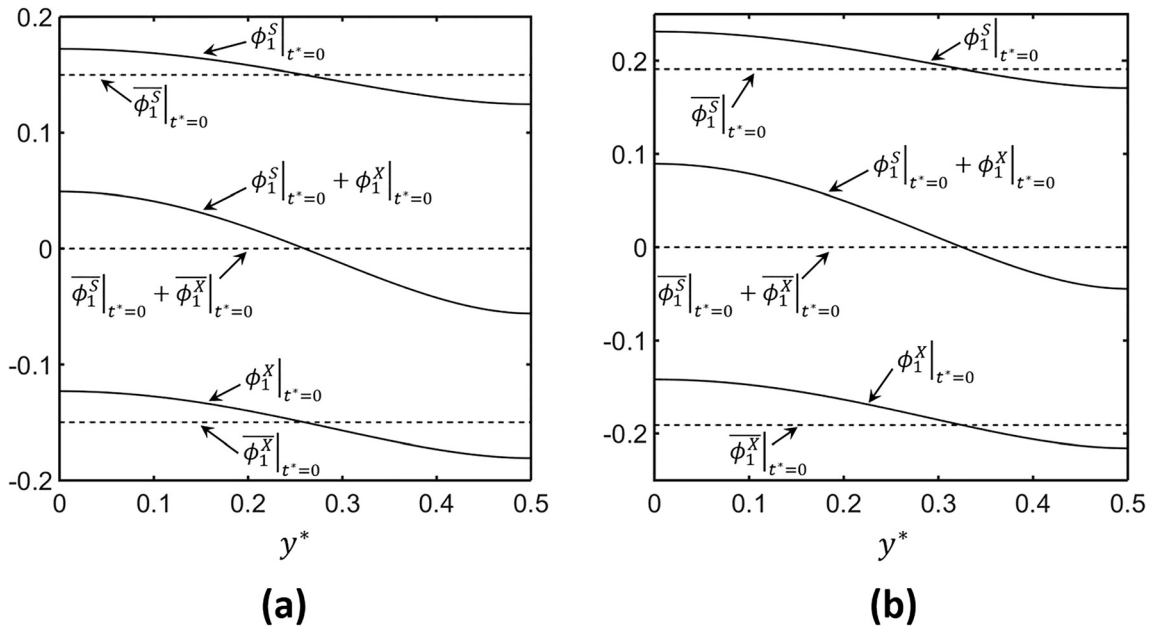

FIG. 4. Spatial variation in ϕ_1^S and ϕ_1^X (solid line) across the y^*-coordinate at $t^* = 0$ in a (a) parallel-plate device and (b) cylindrical capillary when $Pe_S = 10$, $Pe_X = 8$, $Pe_p = 3$, $\alpha = 0.8$, $Da = 3$, and $K_{eq} = 1$. The dotted lines in the sub-figures refer to the spatial average value of the corresponding quantity under the same conditions.

area of the column and hence have the factor $4/\pi$ multiplying the corresponding contributions for a cylindrical capillary. The contribution independent of t^* on the other hand, not only includes similar factors in Eq. (8) but also some mathematical functions, e.g., Bessel functions, which are different from those that describe ϕ_1^S and ϕ_1^X in a parallel-plate device. In Fig. 4, the variation in the time-independent components of ϕ_1^S, ϕ_1^X and $\phi_1^S + \phi_1^X$ across the y^*-coordinate in a parallel-plate device and a cylindrical capillary has been presented by simply plotting their values at $t^* = 0$. These quantities referred to as $\phi_1^S|_{t^*=0}$, $\phi_1^X|_{t^*=0}$ and $\phi_1^S|_{t^*=0} + \phi_1^X|_{t^*=0}$ in the figure are seen to decrease monotonically when the channel/capillary walls are approached moving from the center of the duct. This trend is simply a consequence of the parabolic pressure-driven flow profile advecting S and X faster along the center of the analysis column than around the channel/capillary walls. As a result, all contributions to ϕ_1^S and ϕ_1^X independent of t^* scale with Pe_p consistent with the Taylor–Aris zone-dispersion theory for a pressure-driven flow system. Based on Eqs. (7) and (8), the spatially averaged values for the functions $\phi_1^S|_{t^*=0}$, $\phi_1^X|_{t^*=0}$, and $\phi_1^S|_{t^*=0} + \phi_1^X|_{t^*=0}$ may be further shown to be given by $\overline{\phi_1^S}|_{t^*=0} = -\overline{\phi_1^X}|_{t^*=0} = 4^n K_{eq}(Pe_s - \alpha Pe_X)/\left[\pi^n Da(1+K_{eq})^3\right]$ yielding $\overline{\phi_1^S}|_{t^*=0} + \overline{\phi_1^X}|_{t^*=0} = 0$ which have all been marked as dotted lines in Fig. 4 for reference. As before, the cases $n=0$ and $n=1$ in the above expressions for $\overline{\phi_1^S}|_{t^*=0}$ and $\overline{\phi_1^X}|_{t^*=0}$ correspond to the results for a parallel-plate device and cylindrical capillary, respectively. In this situation, the quantity $\overline{\phi_1^S}|_{t^*=0} > \overline{\phi_1^X}|_{t^*=0}$ when $Pe_S > Pe_X$ and vice versa consistent with the physical description of the system noted above.

The spatial variance of the sample zone (σ^2) may be finally evaluated by solving Eq. (4) for $k = 2$ to yield

$$\frac{\sigma^2}{d^2} = \left(\frac{m_2^S + m_2^X}{m_0^S + m_0^X}\right) - \left(\frac{m_1^S + m_1^X}{m_0^S + m_0^X}\right)^2 = 2\left(\frac{D_{\text{eff}}}{D_S}\right)t^* + \frac{\delta^2}{12},$$

$$\begin{aligned}\left.\frac{D_{\text{eff}}}{D_S}\right|_{n=0} &= \frac{1+\alpha K_{eq}}{1+K_{eq}} + \frac{K_{eq}(Pe_S - \alpha Pe_X)^2}{Da(1+K_{eq})^3} + \frac{(1+K_{eq})Pe_p^2}{210(1+\alpha K_{eq})} \\ &+ \frac{(1-\alpha)^2 K_{eq} Pe_p^2}{5Da(1+K_{eq})(1+\alpha K_{eq})^2} - \frac{12\alpha(1-\alpha)^2 K_{eq} Pe_p^2}{Da^2(1+K_{eq})(1+\alpha K_{eq})^3} \\ &+ \frac{72\alpha^2(1-\alpha)^2 K_{eq} Pe_p^2}{Da^3(1+K_{eq})(1+\alpha K_{eq})^4}\left[\lambda\coth\left(\frac{\lambda}{2}\right) - 2\right], \qquad (9)\end{aligned}$$

$$\begin{aligned}\left.\frac{D_{\text{eff}}}{D_S}\right|_{n=1} &= \frac{1+\alpha K_{eq}}{1+K_{eq}} + \frac{K_{eq}(Pe_S - \alpha Pe_X)^2}{Da(1+K_{eq})^3} + \frac{(1+K_{eq})Pe_p^2}{192(1+\alpha K_{eq})} \\ &+ \frac{(1-\alpha)^2 K_{eq} Pe_p^2}{3Da(1+K_{eq})(1+\alpha K_{eq})^2} - \frac{32\alpha(1-\alpha)^2 K_{eq} Pe_p^2}{Da^2(1+K_{eq})(1+\alpha K_{eq})^3} \\ &\times \frac{256\alpha^2(1-\alpha)^2 K_{eq} Pe_p^2}{Da^3(1+K_{eq})(1+\alpha K_{eq})^4}\left[\frac{\lambda I_2(\lambda/2)}{I_1(\lambda/2)}\right],\end{aligned}$$

where D_{eff} and $\delta^2/12$ refer to the effective or Taylor–Aris dispersion coefficient and sample variance at $t^* = 0$, respectively. The above equation establishes that the presence of a steady pressure-driven flow in an msACE system produces the typical linear increase in σ^2 with time in the Taylor–Aris dispersion limit.[12,20] Moreover, while the mathematical expressions describing D_{eff} in a parallel-plate device ($n = 0$) and cylindrical capillary ($n = 1$) are quite similar, the differences in their cross-sectional shape and area show up in the different numerical and functional coefficients multiplying some of the terms in Eq. (9). The first term in both these cases originates from the axial diffusion of S and X along the analysis column and only depends on the molecular diffusion coefficients for these two species as well as their relative amounts in the system under equilibrium. As may be seen from Fig. 5(a), this contribution labeled by the number 1 asymptotes to the values of 1 and α as $K_{eq} \to 0$ and ∞, respectively, varying monotonically across these limits. In addition, the noted variation does not depend on the cross-sectional geometry or area of the analysis column yielding identical results for $n = 0$ and 1. The second term contributing to D_{eff} arises due to a difference in the electrophoretic velocity of S and X which causes the two species to separate as they migrate through the analysis column. As a result, this contribution increases with the noted velocity differential, i.e., $U_S - U_X$ proportional to $Pe_S - \alpha Pe_X$, as well as the reaction time scales in the system, i.e., $1/k_a$ and $1/k_d$ proportional to $1/K_{eq}$ and $1/Da$, respectively. In Fig. 5(a), the variation in this second term (labeled by the number 2) as a function of K_{eq} has been included which shows the noted quantity to vanish when $K_{eq} \to 0$ or ∞. This trend arises as only one of the reacting species can exist at these limits eliminating the separation between S and X in the system. Moreover, the contribution of this second term to D_{eff} is identical for the cases $n = 0$ and 1 implying it to be independent of the cross-sectional shape and area of the analysis column. Furthermore, this quantity assumes a maximum value of $4(Pe_S - \alpha Pe_X)^2/(27Da)$ when $K_{eq} = 1/2$ and therefore dominates the contribution arising from axial diffusion of S and X only when $Pe_S - \alpha Pe_X \gg 3\sqrt{(\alpha+2)Da}/2$ for $Da/(Pe_S - \alpha Pe_X) \ll K_{eq} \ll (Pe_S - \alpha Pe_X)/(\alpha Da)$.

While the first two terms contributing to D_{eff} in Eq. (9) have been previously investigated in the literature, the remaining ones are unexplored, and capture the effect of a steady pressure-driven flow on band broadening in an msACE system. Noticeably, this latter contribution scales with the square of Pe_p in the Taylor–Aris dispersion limit consistent with previous descriptions of zone dispersion in pressure-driven systems.[12,20] As may be noted, among the four additive terms constituting this contribution, only one does not depend on the reaction kinetics and arises solely due to limited transverse diffusion of S and X across the flow streamlines moving with different velocities. The noted term independent of Da closely matches that described by Aris in his seminal work with a numerical coefficient determined by the cross-sectional shape of the analysis column.[12] The variation of this term with K_{eq} has been included in Fig. 5(a) (labeled by the numbers 3 and 4) which shows it to asymptote to $Pe_p^2/210$ and $Pe_p^2/192$ for a parallel-plate device and cylindrical tube, respectively, for small values of the equilibrium constant. The noted term then varies monotonically with an increase in the magnitude of K_{eq} before plateauing to the values of $Pe_p^2/(210\alpha)$ and $Pe_p^2/(192\alpha)$ for $n = 0$ and 1, respectively, as $K_{eq} \to \infty$. In this situation, while this band broadening component arising from pressure-drive flow and independent of Da remains similar in magnitude in the parallel-plate device ($n = 0$) and cylindrical tube ($n = 1$) under all conditions, its significance relative to the component originating from axial diffusion depends on the parameters α and β where $\beta = Pe_p/\sqrt{210}$ and $Pe_p/\sqrt{196}$ for $n = 0$ and 1, respectively. When β assumes a value between α and 1, the two contributions equal each other [see Fig. 5(a)] at $K_{eq} = (\beta - 1)/(\alpha - \beta)$ with the

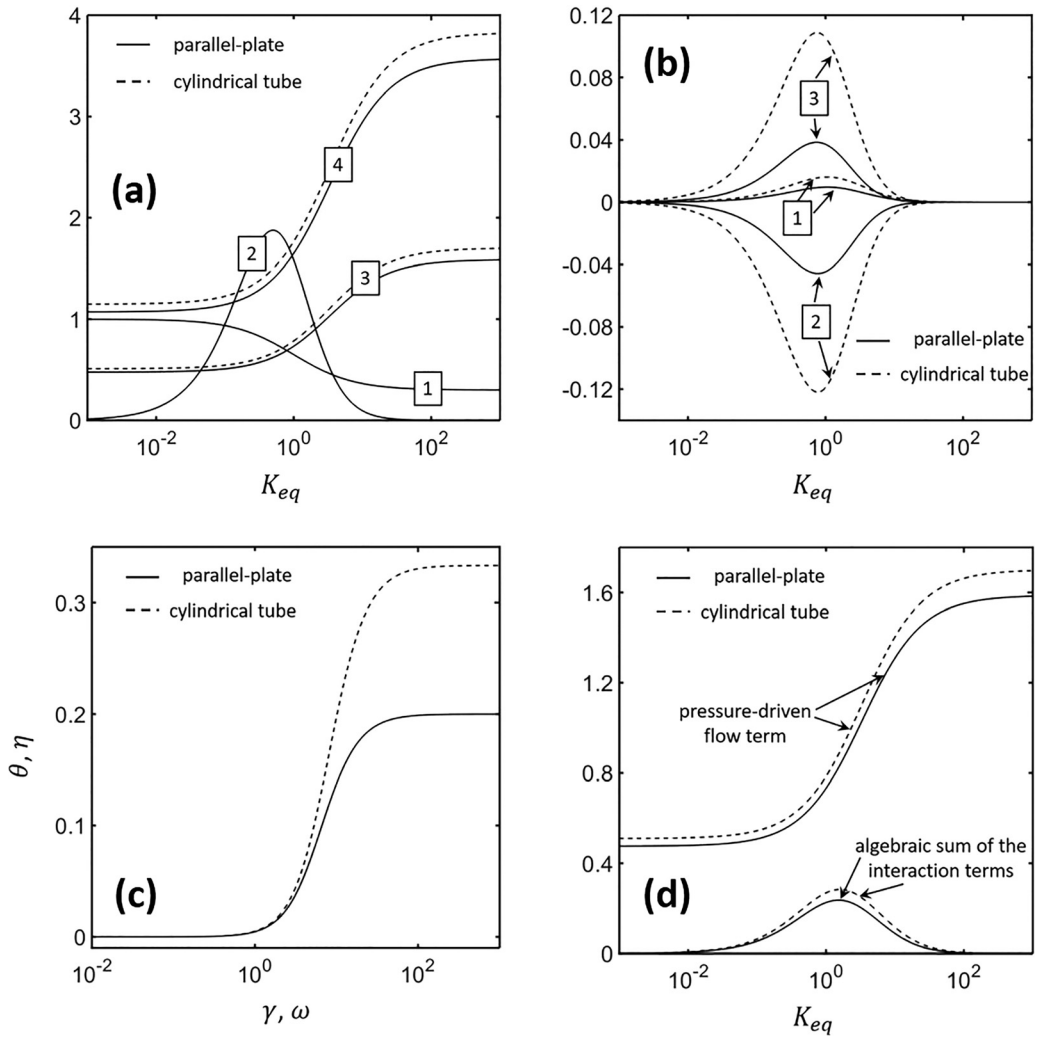

FIG. 5. (a) Variation in the first three terms contributing to D_{eff} in Eq. (9) with the first and second terms labeled by the numbers 1 and 2, respectively, when $Pe_S = 50$ and $Pe_X = 40$. The curves labeled by the numbers 3 and 4 represent the third term for the situations when β assumes a value between α and 1 (choosing $Pe_p = 10$) and when it does not (choosing $Pe_p = 15$), respectively. (b) Factors multiplying Pe_p^2 for the interaction terms contributing to D_{eff} in Eq. (9). (c) Variation in the quantities θ and η with $\gamma = \sqrt{Da/\alpha}$ and $\omega = \sqrt{K_{eq}Da}$, respectively, that describe the behavior of the algebraic sum of the interaction terms in the limits $K_{eq} \to 0$ and ∞. Note that the dependence of θ on γ and η on ω are identical to each other, and are therefore described by the same curves. (d) Relative magnitudes of the pressure-driven flow contribution independent of Da and the algebraic sum of the interaction terms when $Pe_p = 10$. All sub-figures were plotted choosing $\alpha = 0.3$ and $Da = 3$.

former dominating the latter when $\beta \gg 1$ for $K_{eq} \ll 1$ and $\beta/\alpha \gg 1$ for $K_{eq} \gg 1$. If β does not fall within the noted range, the two contributions never equal each other with the former dominating the latter when $\beta, \beta/\alpha \gg 1$ and vice versa.

In order to understand the origin for the last three terms contributing to D_{eff} in Eq. (9), the factors multiplying Pe_p^2 from these contributions have been plotted for a parallel-plate device and cylindrical tube in Fig. 5(b). As may be seen from the figure, these factors vanish both in the limits of $K_{eq} \to 0$ and ∞ similar to the contribution arising from the velocity differential between S and X, i.e., $U_S - U_X$. This behavior combined with the dependence on Pe_p indicates that the noted terms originate from an interplay between the velocity differential $U_S - U_X$ and the pressure-driven flow field in the system. Not surprisingly, these interaction terms also vary inversely with Da, although to different extents, and algebraically sum up to a value greater than zero under all operating conditions. In the limit $K_{eq} \to 0$ for example, their algebraic sum may be expressed as $(1-\alpha)^2 K_{eq} Pe_p^2 \theta / Da$ with $\theta = 1/5 - 12/\gamma^2 + 72[\gamma \coth(\gamma/2) - 2]/\gamma^4$ and $\theta = 1/3 - 32/\gamma^2 + 256\, I_2(\gamma/2)/[\gamma^3 I_1(\gamma/2)]$ for the parallel-plate device and cylindrical capillary, respectively, where $\gamma = \sqrt{Da/\alpha}$. In this situation, the additional band broadening due to the interaction terms decays linearly with K_{eq} for small values of the pseudo first-order equilibrium constant. Moreover, the quantity θ is found to be increasing monotonically with larger values of γ for both the parallel-plate device and cylindrical capillary as shown in Fig. 5(c). While θ vanishes as γ approaches zero both when $n = 0$ and 1, this quantity asymptotes to the values to $1/5$ and $1/3$ for the

parallel-plate device and cylindrical capillary, respectively, as $\gamma \to \infty$. In the opposite limit when $K_{eq} \to \infty$, the algebraic sum of the interaction terms may be written as $(1-\alpha)^2 Pe_p^2 \eta / \left(\alpha^2 K_{eq}^2 Da\right)$ with $\eta = 1/5 - 12/\omega^2 + 72[\omega \coth(\omega/2) - 2]/\omega^4$ and $\eta = 1/3 - 32/\omega^2 + 256\, I_2(\omega/2)/\left[\omega^3 I_1(\omega/2)\right]$ for the parallel-plate device and cylindrical capillary, respectively, where $\omega = \sqrt{K_{eq} Da}$. Notice that although the functional dependence of θ and η on γ and ω are identical, the operating parameters K_{eq}, α and Da relate to γ and ω differently. In fact, the quantity λ simply equals γ and ω when $K_{eq} \to 0$ and ∞, respectively.

Finally, the relative magnitude of the pressure-driven flow contribution independent of Da has been compared to the algebraic sum of the interaction terms in Fig. 5(d) for a choice of $Pe_p = 10$. As evident from the figure, the latter is found to be significantly smaller compared to the former for situations considered in this article, i.e., $t^* \gg 1$, $Da \gtrsim 1$. Moreover, the difference between the two contributions increases for larger values of Da as the interaction terms vary inversely with the Damköhler number in the system. In this situation, the pressure-driven flow contribution independent of Da can be expected to dominate the additional band broadening in msACE systems arising from a pressure-gradient at least in the Taylor–Aris dispersion limit with fast binding kinetics. In Fig. 6, we have included results from numerical simulations performed using the COMSOL Multiphysics package that validates some of the predictions of the analytical model. However, these results match the analytic predictions within 2% only in the Taylor–Aris dispersion limit. At shorter time scales, the dispersion coefficient (D_{eff}) is seen to assume a value lower than its steady-state limit [see Fig. 6(a)] at least for the initial condition outlined in Eq. (1). For comparison purposes, the temporal evolution of the Taylor–Aris dispersion coefficient as predicted by Gill and Sankarasubramanian[22] for simple pressure-driven flow through a tube has been also included in Fig. 6(a) (dashed line). As may be noted, the steady-state limit for this dispersivity is quite different in the two cases in spite of the identical Pe_p value chosen for them. This mismatch occurs due to the additional band broadening contributions arising from the differential in the electrophoretic velocities of S and X as well as the chemical interactions between them. Not surprising however, the timescale over which D_{eff}/D_S attains steady-state in Gill and Sankarasubramanian's work is quite similar to that in the msACE system considered here which assumes fast chemical kinetics relative to diffusion, i.e., $Da(1+K_{eq}) \gg 1$. Nevertheless, the dispersion dynamics is somewhat slower in the latter case likely due to a complex interplay between molecular diffusion and the reaction process.

While the mathematical formulation described here has been applied to evaluating the spatial variance of a sample zone in an msACE system, it can be also extended to calculating the higher order moments of the sample concentration profile, e.g., skewness, kurtosis, etc.[12] However, the present analysis is only valid for assays in which the residence time for the analyte molecules in the analysis column is much larger than their characteristic diffusion time across the channel cross section, i.e., $\ell/(u_S + u_X) \gg d^2/D_S$, where ℓ denotes the length of the analysis column. Moreover, this mathematical model ignores the effect of the channel sidewalls on the pressure-driven flow profile and hence on the hydrodynamic dispersion component of the sample zone.[23] Furthermore, it does not account for any additional band broadening introduced by other non-idealities, e.g., Joule heating,[24,25] electromigration dispersion,[26] wall adsorption,[27] etc., in the system. Nevertheless, the present analysis can be highly useful in estimating

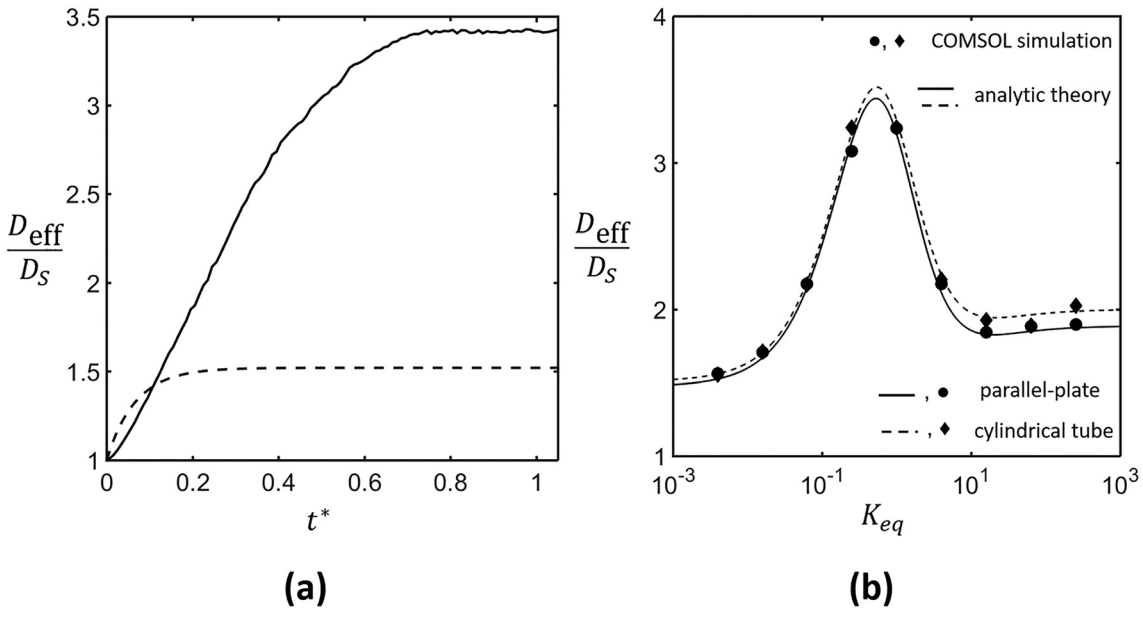

FIG. 6. (a) Temporal variation in the Taylor–Aris dispersion coefficient as predicted by the COMSOL simulations for a cylindrical-tube when $K_{eq} = 0.25$. The dashed line corresponds to the temporal evolution of the Taylor–Aris dispersivity as predicted by Gill and Sankarasubramanian[22] for simple pressure-driven flow through a tube when $Pe_p = 10$. (b) Comparison of COMSOL simulation results with the predictions of the analytic theory. All results included in the sub-figures for the msACE system correspond to the situation when $Pe_S = 50$, $Pe_X = 40$, $Pe_p = 10$, $\alpha = 0.8$, and $Da = 3$.

band broadening in msACE systems with a pressure-gradient applied intentionally or unintentionally along the analysis column. Furthermore, it establishes a mathematical framework for analyzing the influence of channel sidewalls and other non-idealities on analyte transport in the Taylor–Aris dispersion limit.

IV. CONCLUSIONS

In conclusion, the present work outlines an analytical framework that can accurately quantitate analyte migration and dispersion in msACE systems with a steady pressure-gradient applied along the analysis column. It predicts that while such pressure-gradients alter the zone migration rate by the area-averaged pressure-driven flow velocity in the system, its effect on zone dispersion is more complicated and can be quantitated using four additive terms in the Taylor–Aris dispersion limit. All of these terms are further determined to scale with the square of the Péclet number calculated based on the area averaged pressure-driven flow velocity (U_p) and start dominating the overall zone dispersion in the system when U_p exceeds about 25% of the electrokinetic velocities of the analyte species. Moreover, the analytical expressions establish that the first of these terms arises just from the parabolic flow profile of the pressure-driven flow component and is independent of the binding kinetics, whereas the other three contributions, referred to as the interaction terms in this analysis, scale inversely with the Damköhler number and vanish in the limit of both large and small values of the equilibrium constant. These findings are significant in understanding and better designing msACE assays with a pressure-gradient applied intentionally or unintentionally along the analysis column. Moreover, the mathematical framework outlined here may be extended to quantitate the influence of other factors, e.g., Joule heating, electromigration dispersion, etc., relevant to the practical implementation msACE assays and will be explored in future studies. It must be noted that although sample transport under transient conditions, i.e., $t^* \lesssim 1$ is also a topic of high significance in msACE assays,[28] this work has been restricted to results obtained in the Taylor–Aris dispersion limit to preserve its focus and simplicity. The author plans to discuss sample transport in msACE systems under transient conditions in a separate manuscript to be able to present a comprehensive analysis of those results.

SUPPLEMENTARY MATERIAL

See the supplementary material for mathematical derivation of the solutions to Eqs. (3) and (4) when $k = 0,\ 1,$ and 2.

ACKNOWLEDGMENTS

This research work was supported by funds from the National Science Foundation and Wyoming INBRE program through Grant Nos. CHE-1808507 and P20GM103432, respectively.

AUTHOR DECLARATIONS

Conflict of Interest

The author declares no competing financial interest.

DATA AVAILABILITY

The data that support the findings of this study are available from the corresponding author upon reasonable request.

REFERENCES

[1]K. Vuignier, J. Schappler, J. L. Veuthey, P. A. Carrupt, and S. Martel, "Drug-protein binding: A critical review of analytical tools," Anal. Bioanal. Chem. **398**, 53–66 (2010).
[2]M. Jing and M. T. Bowser, "Methods for measuring aptamer-protein equilibria: A review," Anal. Chim. Acta **686**, 9–18 (2011).
[3]T. M. Squires and S. R. Quake, "Microfluidics: Fluid physics at the nanoliter scale," Rev. Mod. Phys. **77**, 977–1026 (2005).
[4]A. C. Moser, S. Trenhaile, and K. Frankenberg, "Studies of antibody-antigen interactions by capillary electrophoresis: A review," Methods **146**, 66–75 (2018).
[5]Y. Wang, D. I. Adeoye, E. O. Ogunkunle, I.-A. Wei, R. T. Filla, and M. G. Roper, "Affinity capillary electrophoresis: A critical review of the literature from 2018 to 2020," Anal. Chem. **93**, 295–310 (2021).
[6]M. Olabi, M. Stein, and H. Wätzig, "Affinity capillary electrophoresis for studying interactions in life sciences," Methods **146**, 76–92 (2018).
[7]J. Ostergaard and H. Jensen, "Simultaneous evaluation of ligand binding properties and protein size by electrophoresis and Taylor dispersion in capillaries," Anal. Chem. **81**, 8644–8648 (2009).
[8]A. Bielejewska, A. Bylina, K. Duszczyk, M. Fialkowski, and R. Holyst, "Evaluation of ligand-selector interaction from effective diffusion coefficient," Anal. Chem. **82**, 5463–5469 (2010).
[9]H. Jensen and J. Ostergaard, "Flow induced dispersion analysis quantifies noncovalent interactions in nanoliter samples," J. Am. Chem. Soc. **132**, 4070–4071 (2010).
[10]L. Leclercq, S. Reinhard, J. Chamieh, M. Doblinger, E. Wagner, and H. Cottet, "Fast characterization of polyplexes by Taylor dispersion analysis," Macromolecules **48**, 7216–7221 (2015).
[11]K. Miyabe and N. Suzuki, "Moment analysis theory for kinetic study of intermolecular interaction by affinity capillary electrophoresis," Bull. Chem. Soc. Jpn. **89**, 746–753 (2016).
[12]R. Aris, "On the dispersion of a solute in a fluid flowing through a tube," Proc. R. Soc. A **235**, 67–77 (1956).
[13]K. Miyabe, R. Takahashi, and Y. Shimazaki, "Kinetic study of interaction between solute molecule and surfactant micelle," Anal. Sci. **31**, 1019–1025 (2015).
[14]D. Dutta, "Transport of charged samples in fluidic channels with large zeta potentials," Electrophoresis **28**, 4552–4560 (2007).
[15]H. Brenner and D. A. Edwards, *Macro-Transport Processes* (Butterworth-Heinemann, Boston, 1993), pp. 65–154.
[16]R. B. Bird, W. E. Stewart, and E. N. Lightfoot, *Transport Phenomenon*, 2nd ed. (John Wiley & Sons, 1960).
[17]D. Dutta, "A method-of-moments formulation for describing hydrodynamic dispersion of analyte streams in free-flow zone electrophoresis," J. Chromatogr. A **1340**, 134–138 (2014).
[18]D. Dutta, "An analytic description of electrodynamic dispersion in free-flow zone electrophoresis," J. Chromatogr. A **1404**, 124–130 (2015).
[19]A. Adrover, C. Passaretti, C. Venditti, and M. Giona, "Exact moment analysis of transient dispersion properties in period media," Phys. Fluids **31**, 112002 (2019).
[20]G. Taylor, "Dispersion of soluble matter in solvent flowing slowly through a tube," Proc. R. Soc. A **219**, 186–203 (1953).
[21]Y. Daneshbod, J. D. Sterling, and A. Nadim, "Moment analysis of near-equilibrium binding interactions during electrophoresis," Phys. Rev. E **76**, 051922 (2007).
[22]W. N. Gill and R. Sankarasubramanian, "Exact analysis of unsteady convective diffusion," Proc. R. Soc. A **316**, 341–350 (1970).
[23]D. Dutta, "Solutal transport in rectangular nanochannels under pressure-driven flow conditions," Microfluid. Nanofluid. **10**, 691–696 (2011).
[24]D. Dutta, "Joule heating induced stream broadening in free-flow zone electrophoresis," Electrophoresis **39**, 760–769 (2018).
[25]D. Dutta, "Effect of channel sidewalls on Joule heating induced sample dispersion in rectangular ducts," Int. J. Heat Mass Transfer **93**, 529–537 (2016).
[26]S. Ghosal and Z. Chen, "Electromigration dispersion in a capillary in the presence of electro-osmotic flow," J. Fluid Mech. **697**, 436–454 (2012).
[27]Z. H. Kou and M. Dejam, "Dispersion due to combined pressure-driven and electro-osmotic flows in a channel surrounded by a permeable porous medium," Phys. Fluids **31**, 056603 (2019). Article no: 056603
[28]L. T. Cherney and S. N. Krylov, "Two-peak approximation in kinetic capillary electrophoresis," Analyst **137**, 1649–1655 (2012).